ASIA TURBOMACHINERY & PUMP SYMPOSIUM
23-26 FEBRUARY 2021
SHORT COURSES: 22 FEBRUARY 2021

EFFECT OF FLOW RATE ON THE PERFORMANCE OF A FLOODED-ENDS TILTING-PAD JOURNAL BEARING – EXPERIMENTS AND PREDICTIONS

Luis San Andrés
Mast-Childs Chair Professor

Hardik Jani, Hussain Kaizar
Graduate Research Assistants

Manish Thorat
Senior Engineer
Elliott Group, Jeannette, PA 15644

J. J. Mike Walker '66 Department of Mechanical Engineering, Turbomachinery Laboratory, Texas A&M University, College Station TX 77843-3123

Luis San Andrés performs research in lubrication and rotordynamics, having produced technological advances in hydrostatic bearings for primary power cryogenic turbo pumps, squeeze film dampers for aircraft jet engines, and gas foil bearings for oil-free micro turbomachinery. Luis is a Fellow of ASME and STLE, and a member of the Industrial Advisory Committees for the Texas A&M Turbomachinery Symposia. Dr. San Andrés has educated dozens of graduate students serving the profession. Dr. San Andrés earned a MS in ME from the University of Pittsburgh and a PhD in ME from Texas A&M University. Luis has published over 310 peer-reviewed papers in ASME *journals and various conferences, including* TPS and ATPS. *Several papers are recognized as best in various international conferences.*

Hardik Jani worked as a Graduate Research Assistant at the Turbomachinery Laboratory, Texas A&M University under the guidance of Dr. Luis San Andrés. Mr. Jani revamped a bearing and seal test rig and conducted experiments on various tilting-pad journal bearings for the Elliott Group. Mr. Jani earned a MS degree in Mechanical Engineering from Texas A&M University (2018) and a BE in Mechanical Engineering from Gujarat University, India (2010). Since 2018, Mr. Jani works as a Mechanical Engineer at Honeywell where he manages the design and development of scanning and mobility devices through its full lifecycle.

Hussain Kaizar worked as a Graduate Research Assistant at the Turbomachinery Laboratory, Texas A&M University under the supervision of Dr. Luis San Andrés. Hussain is an Application Engineer and works for the fluid film bearing division of Dover Precision Components. Mr. Kaizar is responsible for rotordynamic analysis of rotating machinery, performing design reviews, analytical studies, and supporting new product development programs related to fluid film bearing. Mr. Kaizar holds an M.S in Mechanical Engineering from Texas A&M University (2019) and BS in Mechanical Engineering from GIK Institute (2014).

Manish Thorat is a Senior Engineer at Elliott Group since 2010. His areas of expertise include rotordynamics, vibration analysis, testing and evaluation of seal designs, squeeze film dampers and fluid film journal bearing design. Mr. Thorat holds one U.S. patent and has co-authored three publications in ASME journals. Mr. Thorat is a member of ASME and STLE. Mr. Thorat earned his MS degree in Mechanical Engineering from Texas A&M University (2010) and BE in Mechanical Engineering from Mumbai University (2007).

ABSTRACT

Rotating machinery relies on engineered tilting-pad journal bearings (TPJB) to provide static load support with minimal drag power losses, relatively low pad temperatures, and ensuring a rotor dynamic stable operation. End users focus on reducing the supplied oil flow rate into a bearing to lower operational costs and to increase drive power efficiency. However, a too low oil flow might significantly rise pads' (Babbitt) temperatures whilst increasing rotor vibrations due to a reduction in damping. The lecture presents measurements of the steady-state and dynamic forced performance of a TPJB, flooded ends, whilst focusing on the influence of oil flow rate, 50% below and 150% above a nominal condition. The spherical pivots test bearing has five pads with offset = 50% and preload ~ 0.40, and slenderness ratio L/D = 0.4. The test conditions include operation with shaft speed to 16 krpm (85 m/s surface speed) and specific static loads to 2.1 MPa under a load-between-pads (LBP) orientation. A turbine oil lubricates the bearing with a speed-dependent flow rate delivered at a constant temperature. Measurements include the journal static eccentricity and attitude angle, the drag toque, the oil exit temperature rise, and the pads' subsurface temperatures at various locations, circumferential and axial. The measured drag power and the lubricant exit temperature rise depend mainly on shaft speed rather than on applied static load. A reduction in oil flow rate to 50% of its nominal magnitude causes a modest increase in journal eccentricity, a 15% reduction in drag power loss, a moderate raise of ~6°C in pads' subsurface temperatures, a slight increase to 6% in the direct stiffnesses, and a decrease of 7% in the direct damping coefficients. Conversely, a 1.5 times increase in oil flow rate causes a slight increase in drag power loss, max. 9 %, a small drop in the pads' temperatures (up to 3°C), a maximum 5% reduction in direct stiffnesses, and a maximum 10% increase in direct damping. The paper also presents comparisons of the experimental results against predictions derived from a thermos-elasto-hydrodynamic (TEHD) lubrication model. The most important finding relates to the measured bearing drag power differing significantly from a conventional estimate derived from the measured oil exit temperature raise and the supplied mass flow rate. In short, the experimental results demonstrate a reduction in flow rate does not produce a significant drop in drag power losses for the test bearing.

INTRODUCTION

High-speed turbomachinery commonly uses tilting-pad journal bearings (TPJBs) to support loads, static and dynamic, and to provide stable rotor-dynamic operation. With an increasing demand for high power machinery, industry strives for efficient oil-lubricated bearings able to perform at high operating speeds and to carry large specific loads. Operation under these conditions increases the bearing drag, and the lubricant and pad temperatures. The lubricant flow carries most of the heat generated; yet a sizable amount of thermal energy is conducted into the bearing pads, journal, and the bearing housing. Note that the pads Babbitt layer imposes an operation temperature limit as the white metal softens at 125-135°C and melts at ~253°C [1]. Thus, an adequate amount of oil flow keeps the bearing pads' temperatures within acceptable limit. However, an excess of oil flow can lead to unwanted churning losses and with no effective cooling of the bearing pads and Babbitt mainly. On the other hand, a too low oil flow rate may denude or starve the pads of much needed lubricant, and thus increases the risk of oil varnish and coking as well as Babbitt melting. Moreover, in evacuated bearings (those having no end seals), oil starvation can degrade their dynamic force coefficients, a loss in damping in particular that can produce sub synchronous speed rotor vibrations (SSV) [2, 3].

The rotating machinery industry aims to increase power delivery with greater mechanical efficiency, and hence supplying just enough amount of oil into a bearing without affecting its performance is paramount. Efforts toward maintaining bearing performance while reducing energy (drag power loss) and flow consumption have been steady since decades ago, as publications from Heshmat and Pinkus [4] in 1985, DeCamillo et.al [5] in 2001, Dmochowski et al. [6] in 2006, and Nichols et al. [7] in 2018.

DeCamillo et al. [2] in 2008 present a vast amount of data on the onset and persistence of shaft SSV induced by poor lubrication in mainly evacuated ends bearings. The whirl frequencies are low in magnitude though covering a broad band, hence their designation as SSV hash. The phenomenon finds a remedy when selecting a flooded bearing configuration, i.e., one with end seals, or an engineered side grooves configuration that brings lubricant from the leading edge into the loaded section having the smallest oil film thickness.

This lecture presents measurements of the steady state and dynamic forced performance in a flooded TPJB whilst focusing on the influence of supplied oil flow rate, below and above a nominal condition (50% and 150%). Moreover, measurement of the driving torque gives directly the bearing s drag power loss and allows comparisons against a power estimation based on the product of supplied flow rate and lubricant temperature rise.

DESCRIPTION OF TEST RIG AND BEARING

Figure 1 depicts a schematic diagram and various views of the test rig. Jani [8] reports on the reconstruction of this test rig and details its major components and operating characteristics. Note the current test rig updates an early configuration used extensively for the experimental evaluation of both oil seals and hydrodynamic bearings, see Ref. [9] for example.

A main test-section affixed to a steel bed plate, a rotor, and a driver air turbine motor make the test rig. A 65 kW-power air turbine motor, supplied with compressed air drives the test shaft through a high-speed bellow coupling, a torque-limiter, and a torque meter. The AISI 4140 steel shaft has a diameter =101.590 at the test bearing section. Two angular contact ball bearings placed in a back-to-

back orientation support the shaft, while two stiff pedestals, 406 mm apart, house the bearings. An oil-mist lubrication system lubricates the ball bearings.

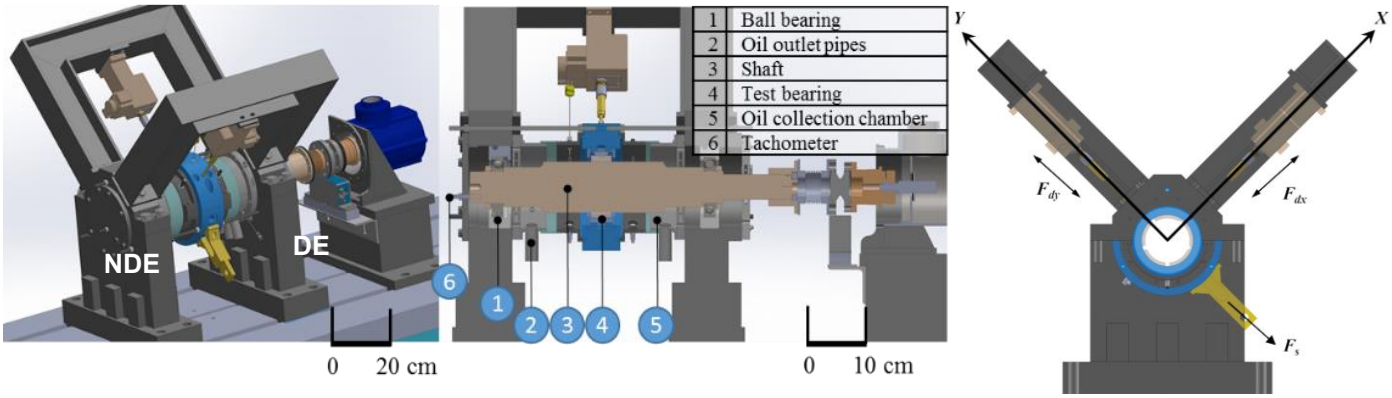

Fig. 1. Isometric view, cross sectional view and front view of test rig.

A bearing stator or housing, made of two matching halves, holds a test bearing and two end caps, and accommodates all associated instrumentation. Lubricant enters at the bottom of the bearing stator and flows through a central groove to lubricate the test bearing. Three pairs of tensioner rods connect the bearing stator to the pedestals. These rods restrain pitch motions of the bearing housing, allow alignment of the bearing with respect to the rotor, and carry the weight of the bearing stator and its components.

A static load mechanism consists of a pneumatic cylinder attached to a soft spring (K_{spring} = 0.26 MN/m) and a cable connected to the bearing housing. The cable when taut applies a load along the (-) *y*-direction. Two electro-hydraulic shaker heads orthogonally mounted along the *x, y* axes attach to the bearing housing via stingers and deliver dynamic loads to the softly mounted test bearing. Each shaker head consists of a hydraulic valve and a linear variable differential transformer sensor. A hydraulic-pump powers a shaker head, while an electronics master-controller precisely sets the stator static and dynamic motions.

Figure 2 shows a front view of the bearing stator and its instrumentation. Two pairs of *(x,y)* eddy-current sensors installed in the end caps measure the relative displacement between the shaft and bearing along the *x* and *y*-axes. Displacement sensors along the same axis (*x* or *y*) allow monitoring the stator pitch and yaw. Two accelerometers record the acceleration of the bearing stator along the *x* and *y* axes. A J-type thermocouple and a strain gauge pressure sensor measure the oil inlet temperature and pressure in the central groove of the stator. Two other similar thermocouples and pressure sensors installed in the end caps record the lubricant exit temperature and pressure on each side of the test bearing. Two force sensors, each attached to a shaker head, measure the applied dynamic forces, and a third force sensor attached to the pneumatic cylinder records the static load. A fifth eddy-current displacement sensor (not shown) faces a key (mark) on the shaft to record its angular speed. A strain-gauge type torque-meter installed in-line with the shaft measures the drive torque.

Table 1 details the test bearing geometry, lubricant properties, and operating conditions under a pressurized (flooded) configuration with static load applied between pads (LBP). Figure 3 shows photographs of the test bearing: a five-pad TPJB (L/D = 0.4) with a ball-in-socket pivot and 50% pivot offset. The test bearing clearance to radius ratio (C_r/R) is ≈ 0.0013, and the pads' preload = 0.42 (on average) at room temperature. The bearing base-ring has two end seals on each side, their clearance is about five or more times that of the bearing with its rotor.

Figure 4 shows the layout of 30 K-type thermocouples instrumented in the five pads of the bearing. The depth of the sensors from the Babbitt surface of each pad is about 2.4 mm. Pads 4 and 5 are the loaded-pads for the LBP orientation. Each pad has six embedded thermocouples; four at arc lengths = 10, 25, 75 and 90% on the bearing mid-plane, and two along the axial direction at the 75% location of the pad arc-length. Note that the designation X-Y for the thermocouple corresponds to X=pad number and Y=location on the pad, one is near to the leading edge and six near to the trailing edge of the pad as shown.

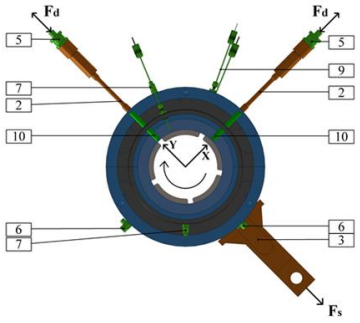

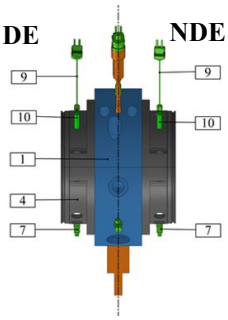

Item no.	Part Name
1	Bearing stator
2	Stinger
3	Static loader yoke
4	Bearing end caps
5	Load cell (force transducer)
6	Accelerometer
7	Pressure sensor
9	Thermocouple
10	Eddy-current sensor

Fig. 2 Front and side views of bearing stator, test bearing, and location of instrumentation.

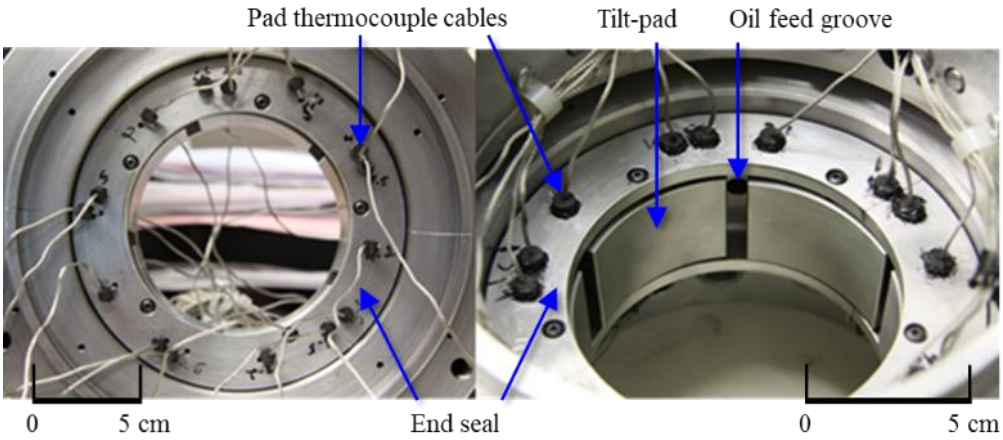

Fig. 3 Photographs of test bearing and thermocouple wires.

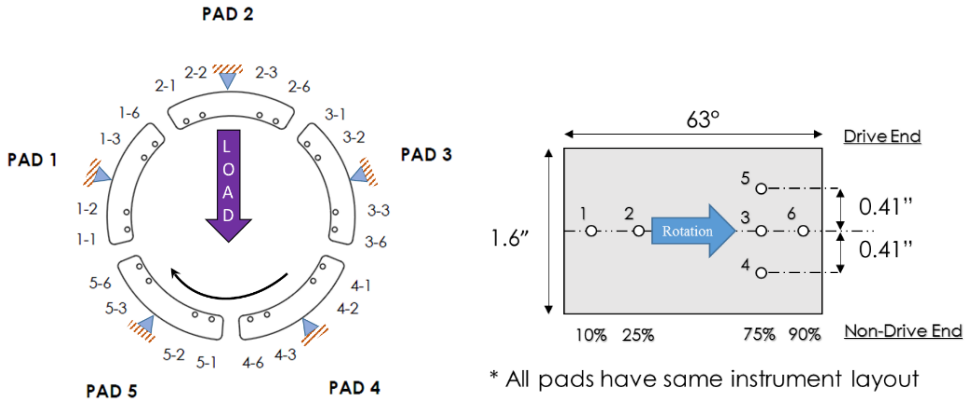

Fig. 4. Bearing pad thermocouple layout in test bearing.

EXPERIMENTAL RESULTS AND DISCUSSION

Measurement of the Bearing Clearance and its Center

Coghlan and Childs [9] detail the procedure to align the bearing stator relative to the shaft and a process to determine the bearing clearance and its center, prior to begin a test and/or immediately after while the rotor is still warm. The shakers push and pull the bearing stator with a light load around the stationary shaft until contact ensues; and the displacement sensors reveal complete periphery (shape) of the bearing clearance, a pentagon for a five-pad bearing. The coordinates of the corners (vertex) and pivots are extracted from the measured clearance shape. A best-fit circle of the derived pivot coordinates delivers an estimated circular bearing clearance and the bearing center. Figure 5 depicts the measured diametrical clearance (C_d), '*cold*' (CC) at room temperature (24°C) and '*hot*' (HC) immediately after completing a test. After continuous operation at 16 krpm the average *hot* clearance (C_d=0.105 mm) at $T \approx 65$°C is

16% smaller in size compared to the *cold* clearance (C_d=0.125 mm) at $T \approx 24$°C. Knowledge of the *hot* clearance is vital to produce accurate predictions of bearing performance.

Table 1. Test bearing geometry, lubricant properties and operating conditions.

Bearing Geometry n_p=5 (pads)	
Shaft diameter, D	101.59 mm
Bearing axial length, L	41 mm
Pad arc length, β_p	63°
material	Steel
mass	0.25 kg
mass moment of inertia about pivot	1.14 kg.cm^2
Pivot offset	50%
Pad preload (m)	0.42 (± 0.03)
Pad nominal radial clearance (C_{pad})	0.112 mm
Bearing nominal radial clearance (C_r)	0.0625 mm
Fluid Properties at oil inlet temperature 49ºC	
Lubricant	ISO VG 32
Viscosity, μ_{in}	19.7 mPa.s
Viscosity temperature coefficient	0.0296/°C
Density	851 kg/m^3
Specific heat coefficient	1980 kJ/(kg K)
Lubricant supply configuration	Flooded
Oil inlet type	Orifice
Operating Conditions	
Applied load range, W	710 – 8,540 N
Specific load range, $W/(LD)$	0.17 – 2.1 MPa
Rotor speed range, Ω	6 – 16 krpm
Surface speed, ½ ΩD	32 m/s - 85 m/s

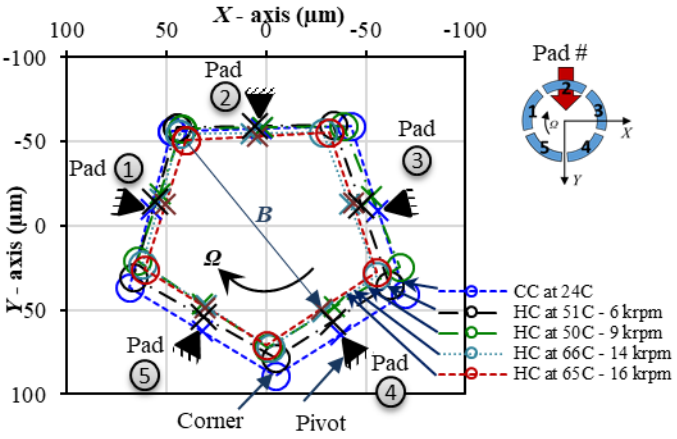

Fig. 5. Bearing clearance measurement conducted at ambient temperature (24ºC) and at hot temperature (50ºC -66ºC) after test with shaft speed.

During a test, lubricant (ISO VG 32) at T_{in} = 49 ± 0.5 °C (120ºF) flows into the bearing with a (shaft speed-dependent) set oil flow rate. Thereafter a control system accelerates the air motor to a pre-determined rotor speed. A combined operation of two heat exchangers, an air-cooled cooler and oil heater, maintain the oil inlet temperature (T_{in}). At the onset of a test, the spinning rotor drags the viscous fluid and warms the oil while the bearing and shaft slowly increase in temperature until achieving a thermal steady state in about 45-60

minutes. Next, the pneumatic loader applies a static load on the bearing as soon as the system achieves the desired rotor speed. For subsequent test points, the time taken to achieve thermal steady state reduces to 10-20 minutes depending on operating conditions.

As an example, Fig. 6 presents a timeline of sensor readings for rotor speed, applied static load and pad # 4 temperature for operation at 6 krpm, as the applied load increases from 700 to 2,800 N. The pad temperature becomes steady in ~t 10-15 minutes after the increase in load. A similar time frame occurred for most other operating conditions. Upon achieving thermal equilibrium for a specific operating condition, the DAQ records and save a full set of data consisting of the load, eccentricity, torque and various oil and pad (30 or so) temperatures.

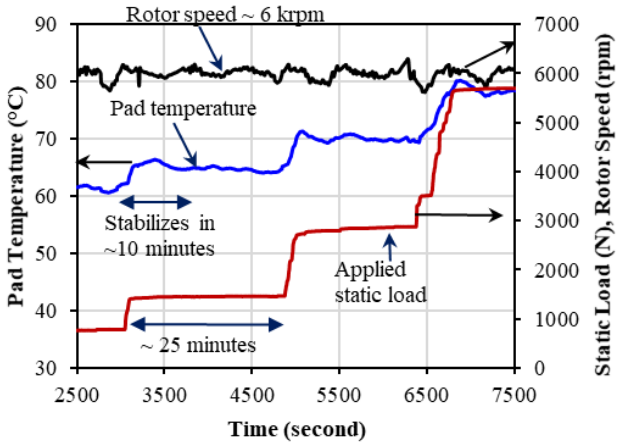

Fig. 6 Example of the timeline of rotor speed (rpm), applied static load (N) and measured temperature (°C) on pad #4 at 75% location for operation at 6 krpm, applied static load from 700 N to 2.8 kN, and nominal flow.

Measured lubricant exit temperatures

The actual supplied flow rates ($\dot{Q}$) are proprietary to the sponsor, albeit any person with a rudimentary knowledge of lubrication should realize the lubricant supply flow rate is proportional to shaft surface speed. After lubricating the pads, warm oil streams at T_{exit} leave the bearing through the end seals and measured by thermocouples on the bearing drive end side (DE) and non-drive end side (NDE), see Fig. 2.

Figure 7 presents the arithmetic average of both DE and NDE sides temperatures versus specific load for operation at five shaft speeds, 6 krpm to 16 krpm or 32 m/s to 85 m/s shaft surface speed, and 100% nominal oil flow rate. The oil exit temperature does not vary significantly with an increase in applied static load but does consistently rise with an increase in shaft speed. The error bars in the figure denote the difference in temperatures measured on the DE and NDE sides (ΔT_{DE} - ΔT_{NDE}).

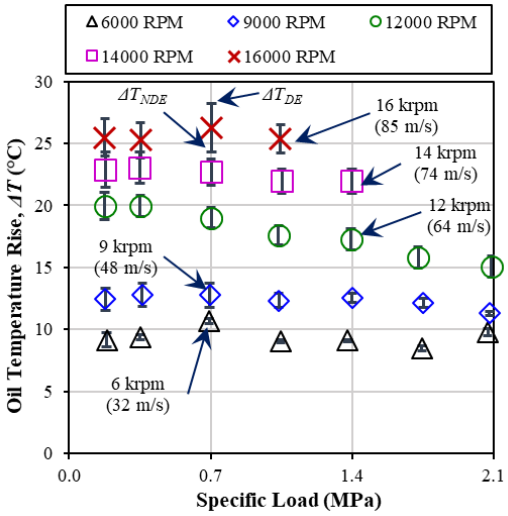

Fig. 7. Measured average oil exit temperature rise, ½(DE+NDE) Δ*T*, vs. specific load for operation at rotor speeds = 6 krpm to 16 krpm (32 m/s-85 m/s) and 100% nominal flow. Oil supply temperature=49°C.

Figure 8 depicts the average oil temperature rise (ΔT) measured at the bearing exit plane for operation with supplied oil flow rates at 27%, 50%, 100% and 150% of nominal flow. The test conditions include operation at a surface speed of 48, 64 and 74 m/s (9, 12 and 14 krpm), and under a specific load of 0.35 and 1.0 MPa. On reducing the oil flow rate to 50% of nominal, ΔT increases by 4°C, whereas on increasing the oil flow rate to 150% of nominal, ΔT lowers by 2 °C for operation at 74 m/s and under specific load of 0.35 MPa and 1.0 MPa. ΔT results recorded when changing the oil flow rate for operation at 48 m/s and 64 m/s are very similar to those measured at 74 m/s.

For a single case with 27% of nominal flow at 12 krpm (64 m/s) and under 0.35 MPa specific load, surprisingly ΔT is 8°C lower when compared to ΔT at the nominal (100%) flow rate. However, due to difficulties in controlling the temperature of the bearing housing, do note that the oil supply temperature increased up to 61°C at the bearing entrance for such a low oil flow rate; i.e., the operating conditions are out of the normal test conditions. As per Nicholas in Ref. [1], a reduction in oil flow rate produces a decrease in oil film thickness and thus causes a larger drag torque and a subsequent temperature rise in the oil film. Conversely, an increase in oil flow may lower the oil exit temperature as it carries more thermal energy.

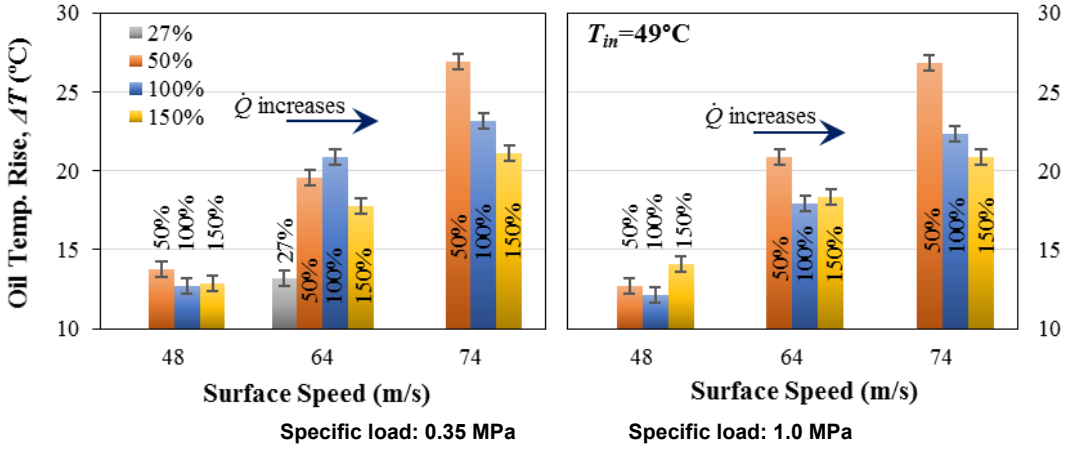

Fig. 8. Measured discharge oil temperature rise ΔT vs. surface speed (48 m/s, 64 m/s and 74 m/s) under specific loads (a) 0.35 MPa and (b) 1.0 MPa. Bearing supplied with 50%, 100%, and 150% oil flow rates.

Measured and estimated bearing drag power losses

Engineering practice estimates the bearing drag power loss (P_{est}) from the heat flow carried away by the lubricant [1]:

$$\kappa P_{estimated} = \rho\, C_p\, \dot{Q}\, \Delta T \tag{1}$$

where ρ and C_p are the oil density and specific heat, $\dot{Q}$ is the supplied flow rate, ΔT is the lubricant temperature rise measured at the bearing exit planes, and κ denotes the fraction of power converted into heat and advected by the fluid flow. DeChoudhury and Barth [10] note that oil discharge temperatures may be obscured by the heat flow conducted into the bearing casing (and shaft). Additional heat flows through oil drain lines from the bearing to the discharge oil temperature location can also affect the thermal balance. Presently, as the oil temperatures are measured immediately on the sides of the bearing, heat losses in the discharge flow passages are minimal. For a bearing with end seals (flooded configuration), $\kappa \sim 0.8$ [11].

Incidentally, DeChoudhury and Masters [12], Pettinato and DeChoudhury [13], and Dmochowski and Blair [6], among many practitioners, produce bearing drag power loss estimates based on the measurement of the discharge oil temperature, i.e., Eq, (1). Only DeCamillo and Brockwell [5] report bearing drag power losses derived from measurement of the torque restraining rotation of a bearing housing.

Presently, an in-line torque meter measures the drive torque, and which when multiplied times the rotor angular speed (Ω), delivers the actual drag power loss ($P_{measured}$) in the test bearing. For presentation of the experimental results, define a dimensionless or normalized drag power loss as,

$$\bar{P} = \frac{P_{measured\ or\ estimated}}{P_{lub}} \tag{2}$$

where

$$P_{lub} = \mu_{eff}\, L\, \Omega^2 \frac{D^3}{8C_r}\left(n_p\, \beta_p\right) \tag{3}$$

is a theoretical prediction of the power loss derived from a simple analysis of the Couette flow through the lubricated gap in a bearing

pad. Above n_p=5 and β_p= 1.09 rad (63º) and μ is the oil effective[1] viscosity. Note that $\bar{P}$ ~1 evidences an exact correlation between theory and the given parameter, measured or estimated.

Figure 9 depicts the measured and estimated bearing power loss ($\bar{P}$) vs. specific load (0.17 MPa - 2.1 MPa) for increasing rotor speeds (9 krpm -16 krpm) and with the bearing supplied with the nominal oil flow rate. As is well known, $\bar{P}$ significantly depends on shaft speed though it is nearly independent of applied load. At 9 krpm (48 m/s), $\bar{P}_{measured}$ varies just ~5% with an increase in applied load from 0.17 to 2.1 MPa. Conversely, at 1.0 MPa specific load, $\bar{P}_{measured}$ increases by 45% with an increase in shaft speed from 9 to 16 krpm (48 to 85 m/s).

Overall for most test conditions, $\bar{P}_{measured}$ is within 20% of a prediction using Eq. (6). More distinctive is, however, the significant discrepancy with the power measured directly ($\bar{P}_{measured}$). Do recall the supplied oil flow rate is not constant but proportional to shaft speed, and thus directly influences the estimated $\bar{P}$.

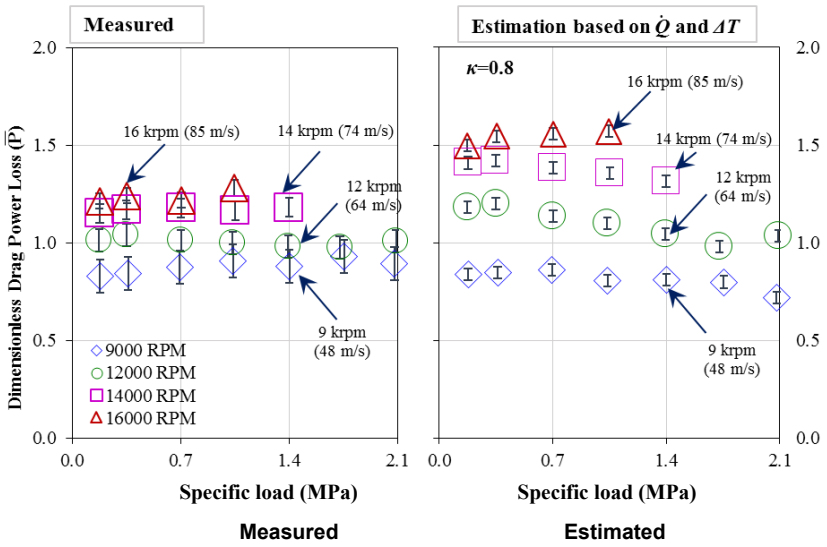

Fig 9. Bearing normalized drag power loss ($\bar{P}$), measured and estimated, vs. specific load for operation at four rotor speeds (9 krpm to 16 krpm). Bearing supplied with (100%) nominal flow rate.

Figure 10 presents a comparison of the measured and estimated drag power loss ($\bar{P}$) for tests conducted at three surface speeds (16 m/s, 32 m/s and 43 m/s), under a 1.0 MPa specific load, and with the bearing supplied with three oil flow rates (50%, 100%, and 150%). On reducing the oil flow rate from 100% to 50% of nominal, $\bar{P}_{measured}$ reduces by ~15 % whereas $\bar{P}_{estimated}$ reduces by ~54%. Conversely, on increasing the oil flow rate from 100% to 150% of nominal value, $\bar{P}_{measured}$ increases by ~9 %; whereas, $\bar{P}_{estimated}$ grows by ~31%. The measurements reveal that $\bar{P}_{measured}$ is less sensitive to the supplied oil flow rate as $\bar{P}_{estimated}$ otherwise shows.

The in-house TEHD model [14,15] predicts a significant reduction in drag power loss by ~20% (average) when reducing the oil flow rate by 50% of nominal. The same model predicts an increase of ~15% in drag power when increasing the oil flow rate by 50%. These results are not shown in the graphs.

The experimental results for the measured drag power loss reveal a deficiency for the overly simplistic Eq. (1) which delivers unusually low power losses as the lubricant flow rate drops. Clearly recording the oil temperature rise across the bearing does not lead to an accurate estimation of the bearing actual drag power loss.

[1] μ_{eff} = f (T_{eff}) is an oil effective viscosity calculated at the *effective temperature* [$T_{eff}=T_{in}+¾\,(T_{exit}-T_{in})$]

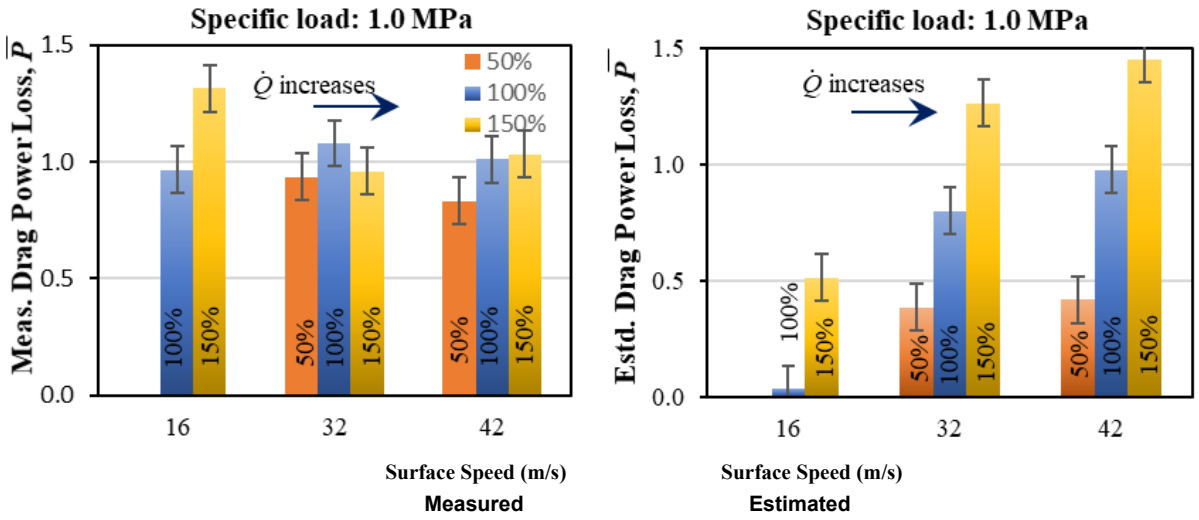

Fig. 10. Bearing normalized drag power loss ($\bar{P}$), measured and estimated, vs. shaft surface speed (16 m/s, 32 m/s and 42 m/s) for operation at 1.0 MPa and three oil flow rates (50%, 100%, and 150%).

Measured journal eccentricity (*e*) vs Sommerfeld # (*S*)

Let the journal eccentricity ratio $\varepsilon = (e/C_r)$ where e is the shaft center displacement and C_r is the bearing *cold* clearance at T=24°C. Figure 11 depicts the loci of shaft displacements, ε_y vs. ε_x, for operation at four rotor speeds and under an increasing specific load (LBP). The displacement (ε_y) along the applied load direction is much larger that the orthogonal displacement (ε_x), and hence the shaft center attitude angle is rather small as expected with a TPJB; refer to Jani [8] for details.

Figure 12 depicts the measured and predicted journal eccentricity ratio (ε) vs. specific load $W/(LD)$ for operation at five rotor speeds (6 krpm-16 krpm) and a nominal (100%) oil flow rate. For operation at the lowest speed (6 krpm), ε increases nonlinearly as the load increases. However, for the largest shaft speed (16 krpm), the shaft eccentricity is significantly smaller and nearly proportional to the applied load. For most operating conditions the TEHD model [14,15] predicts a journal eccentricity agreeing well with the measurements. An exceptional under prediction occurs for operation at 6 krpm (32 m/s) that produces the largest shaft eccentricity as the load increases.

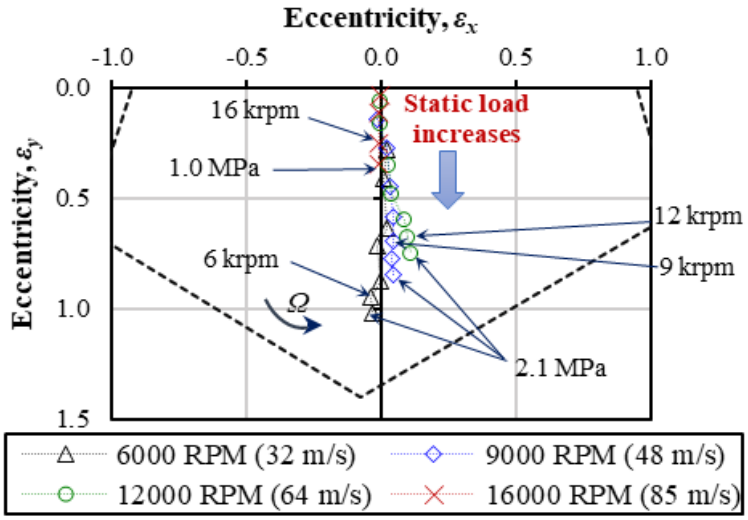

Fig. 11. Locus of measured shaft eccentricity ε_y vs. ε_x for increasing loads (*y* direction) and shaft speeds from 6 krpm (32 m/s) to 16 krpm (85 m/s).

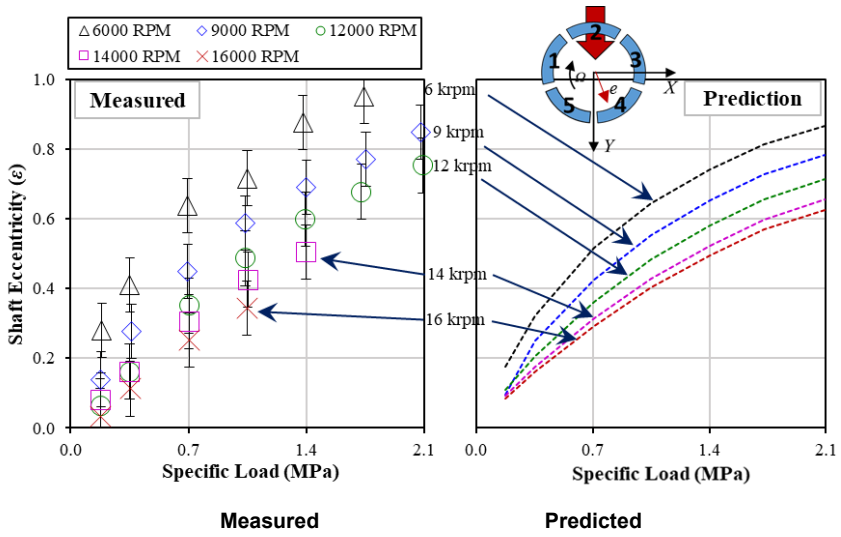

Fig. 12. Test bearing measured and predicted eccentricity ratio (e/C_r) vs. specific load for operation at five rotor speeds (6 krpm to 16 krpm) and nominal flow.

In classical lubrication and engineering practice, the journal eccentricity ratio (ε) correlates with the Sommerfeld number (S)

$$S = \mu_{eff} N \frac{LD}{W}\left(\frac{D}{2C_r}\right)^2 \tag{4}$$

where N is shaft speed in rev/s and W is the applied load. Figure 13 depicts the measured and predicted eccentricity ratio (ε) vs. Sommerfeld #. Operation at a low to moderate rotor speed (< 9 krpm) and under a large specific load (> 1.4 MPa) produces $S < 0.8$, and thus the shaft eccentricity ratio is large ($\varepsilon > 0.78$). The shaft eccentricity decreases as S increases, i.e., with a lesser static load (W) or a higher shaft speed (N).

Both measured and predicted ε follow a similar trend for $S = 0.3$ to 10, and importantly enough, point out to the goodness of the experiments and the validation of the engineering practice. Note that few if any recent publications reporting experimental results for tilting pad bearings show an effort to normalize the data in dimensionless form. Modern practice treats each experimental result as an isolated occurrence and does not help to build general observations and permanent knowledge.

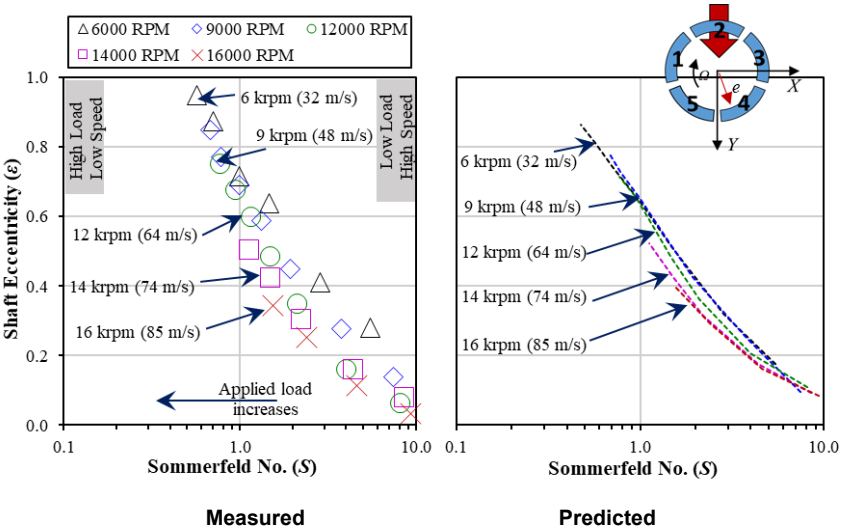

Fig. 13. Measured and predicted shaft eccentricity ratio (e/C_r) vs. Sommerfeld number for operation at various shaft surface speeds (32 m/s to 85 m/s), specific loads (0.17 MPa to 2.1 MPa), and nominal flow rate.

Figure 14 depicts the shaft eccentricity (ε) as a function of shaft surface speed and applied loads (0.35 and 1.0 MPa) while the bearing is supplied with oil flow rates ranging from 27% to 150% of nominal flow. For operation at 12 krpm (64 m/s) and 1.0 MPa, ε increases by 22% at 50% of nominal flow when compared to the eccentricity at the nominal flow. Unexpectedly, ε also increases 9% at the 150% flow condition. Similar patterns of behavior appear for operation at a rotor speed of 9 krpm (48 m/s) and 14 krpm (74 m/s) and with a specific load of 0.35 MPa.

The in-house TEHD model [14,15] predicts ε increases for operation with a reduced oil flow rate (50% of nominal) and decreases with an increase in oil flow (150% of nominal). Hence, the increase in measured shaft eccentricity for operation with 150% of nominal flow remains paradoxical.

Measured Subsurface Temperatures in the Bearing Pads

To exhaustively quantify the thermal performance in the test bearing, a total of 30 embedded thermocouples record the pad sub-surface temperature, as shown in Fig. 4. Note pads # 4 and #5 are the loaded pads under a LBP orientation. For depiction of the measurements define a (dimensionless) pad defect temperature (θ) as,

$$\theta = \frac{T_{pad} - T_{in}}{T_{exit} - T_{in}} = \frac{\Delta T_{pad}}{\Delta T_{rise}} \tag{5}$$

where T_{pad} is the measured pad sub-surface temperature, T_{in} is the oil inlet temperature, and T_{exit} is the oil outlet temperature, averaged from measurements on the left and right sides of the bearing. θ denotes the rise in pad temperature (ΔT_{pad}) with respect to the overall oil temperature rise at the discharge (ΔT_{rise}). For example, a test with ΔT_{rise} = 30ºC and $\theta \approx 2$ denotes an actual pad temperature rise of 60ºC.

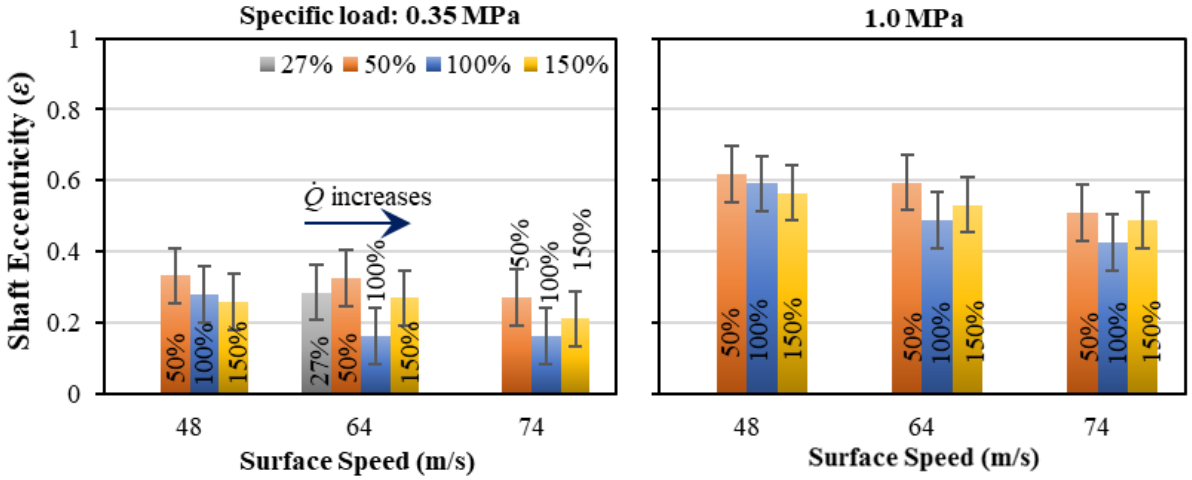

(a) 0.35 MPa load (b) 1.0 MPa load

Fig. 14. Measured shaft eccentricity ratio (ε) vs. shaft surface speed (48 m/s, 64 m/s and 74 m/s) for operation under specific load (a) 0.35 MPa and (b) 1.0 MPa, and oil flow rates at 50%, 100% and 150% of nominal flow.

Figure 15 depicts the pads' measured defect temperature (θ) versus circumferential location for operation at three specific loads (0.35, 1.0 and 2.1 MPa), four rotor speeds (6 krpm -16 krpm 32 m/s-85 m/s]), and 100% nominal lubricant flow. As expected, θ increases from a pad leading edge toward its trailing edge due to viscous shear heating.

With an increase in specific load from 0.35 MPa to 1.0 MPa and then to 2.1 MPa at a surface speed of 32 m/s, the peak defect temperature (θ_{max}) on loaded pad #5 increases from 2.5 to 3.5 and 3.9, respectively. Moreover, with an increase in shaft surface speed from 32 m/s to 85 m/s, under a specific load of 1.0 MPa, θ_{max} reduces from 3.5 to 2.7. Note a low θ for operation at a high shaft speed may be confusing; however, recall that at 85 m/s, the oil temperature rise (ΔT_{oil}) higher by ~16ºC than that at 32 m/s. Hence, the actual pad temperatures (T_{pad}) for operation at high shaft speed are higher.

Do note that the leading edge temperatures for all five pads are not identical for the various operating conditions; hence suggesting an uneven oil flow distribution into each pad and unequal hot oil carry-over coefficients, as argued by Abdollahi and San Andrés [15]. Interestingly, $\theta < 1$ at the leading edge of all five pads indicates enough fresh oil makes the respective fluid films.

Furthermore, on the unloaded pads #1, #2 and #3, an increase in specific load, from 0.35 MPa to 2.1 MPa, produces no significant changes in θ_{max}~4.0 irrespective of the shaft speed. Under a high specific load (> 1.0 MPa), the resistance of the fluid to enter a pad's

leading edge is greater on the loaded pads rather than on the unloaded pads, and which results into more fresh oil flow available on the unloaded pads, thus lowering θ.

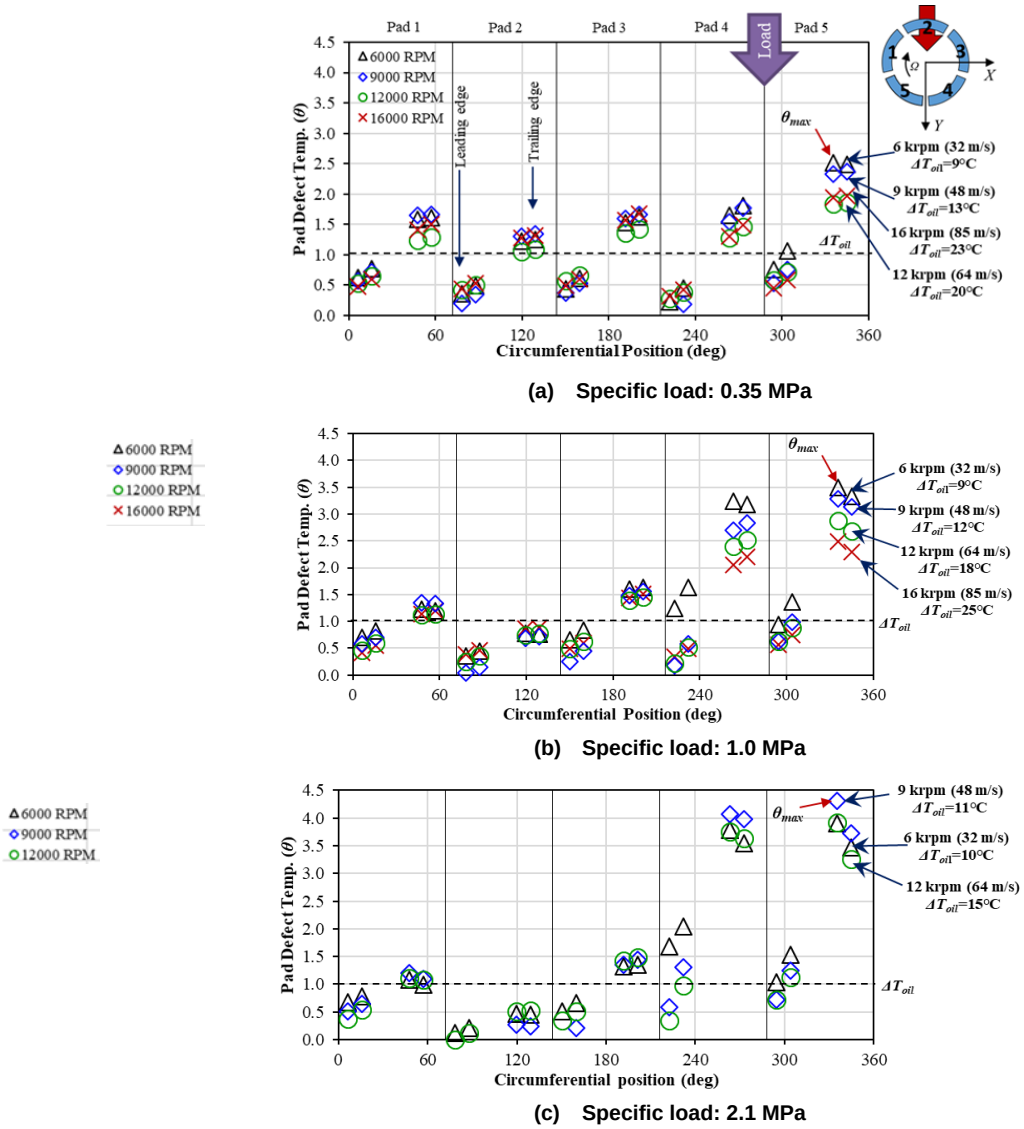

Fig. 15. Measured pad defect temperature (θ) at 20 circumferential locations on bearing mid-plane for operation with specific loads (a) 0.35 MPa, (b) 1.0 MPa and (c) 2.1 MPa. Measurements obtained at four rotor speeds (6 krpm to 16 krpm) and 100% nominal flow rate.

Interestingly enough, for the largest applied load (2.1 MPa), Fig. 15(c) shows $\theta_{max} \sim 4.0$ irrespective of shaft speed (48 m/s – 64 m/s); hence the peak pad temperature can be easily estimated from a measured ΔT_{oil}. Incidentally, Jani [8] also reports measurements of pad subsurface temperatures at two axial locations on the sides of a pad at the 75% pad arc length. Those measurements are omitted for brevity.

Figure 16 presents a comparison of the measured and predicted peak temperature θ_{max} in pad #5 vs. Sommerfeld number (S). Operation at a large S produces a low θ_{max} and vice versa. For example, at $S = 4$, $\theta_{max} \approx 2$ whereas for S=0.5 θ_{max} increases two-fold, $\theta_{max} \approx 4$. The model significantly over predicts θ_{max} for all S for operation below 12 krpm (64 m/s). However, when compared to the measured (θ_{max}), the model does predict accurately for operation at 14 krpm and 16 krpm. It is remarkable that the experimental data collapses within small bounds whereas the predictions show distinct curves. The discrepancy lies likely on the (numerical) evaluation of the exit oil temperature, a result of the mixing of the outlet flow streams leaving the five pads.

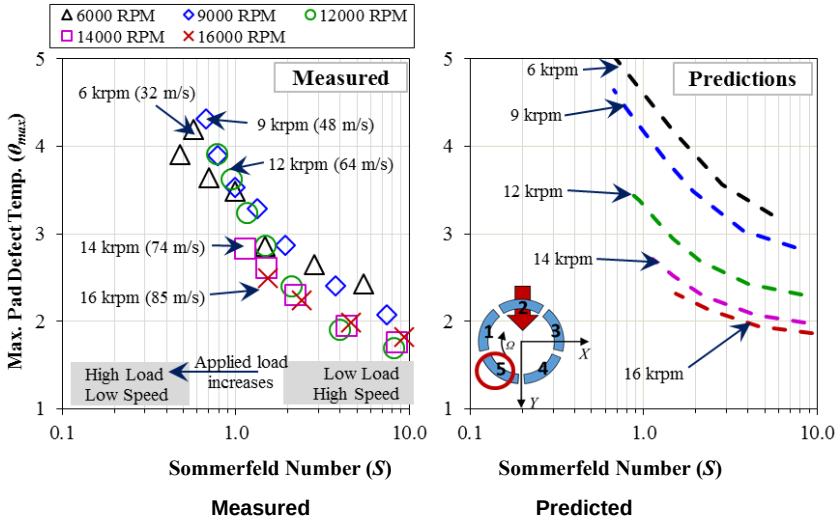

Fig. 16. Peak defect temperature (θ_{max}) in pad #5 vs. Sommerfeld number (S): Measured (left) and predicted (right). Operation at five rotor speeds (6 krpm-16 krpm) under various specific loads (0.17 MPa-2.1 MPa). Bearing supplied with nominal oil flow rate.

Figure 17 depicts a comparison of the measured pads' defect temperature (θ) for operation with a supply oil flow rate at 50%, 100% and 150% of nominal flow. The test data includes two shaft speeds, 9 krpm and 12 krpm, and three specific loads, 0.35 MPa, 0.7 MPa and 1.0 MPa. On changing the oil flow rate to 50% and 150% of the nominal magnitude, θ varies by at most ± 0.3 compared to those θ's recorded at the nominal oil flow rate.

An increase or decrease in θ depends on both the rise in oil temperature and the pad temperature. For operation at shaft speed=9 krpm, θ_{max} ~ 3 - 3.5 on the loaded pads # 4 and #5, while for shaft speed=14 krpm, θ_{max} ~ 2.5 - 3, both at 1.0 MPa load. The physical pad temperatures slightly increase, ~ 5°C max. for a 50% oil flow, while decreasing just ~ 2°C max. with a 150% flow, when compared to the pad temperatures obtained for operation under the nominal oil flow.

In sum, varying the flow rate has a minor effect on the pad defect temperature (θ) [and actual physical temperatures], a feature of the flooded bearing configuration tested.

The in-house TEHD model (results not shown for brevity) predicts a rise in θ_{max} of about 15% on reducing the oil flow rate from 100% to 50% of nominal. On the other hand, the model predicts a decrease in θ_{max} of about 10% on increasing the oil flow rate to 150% of nominal.

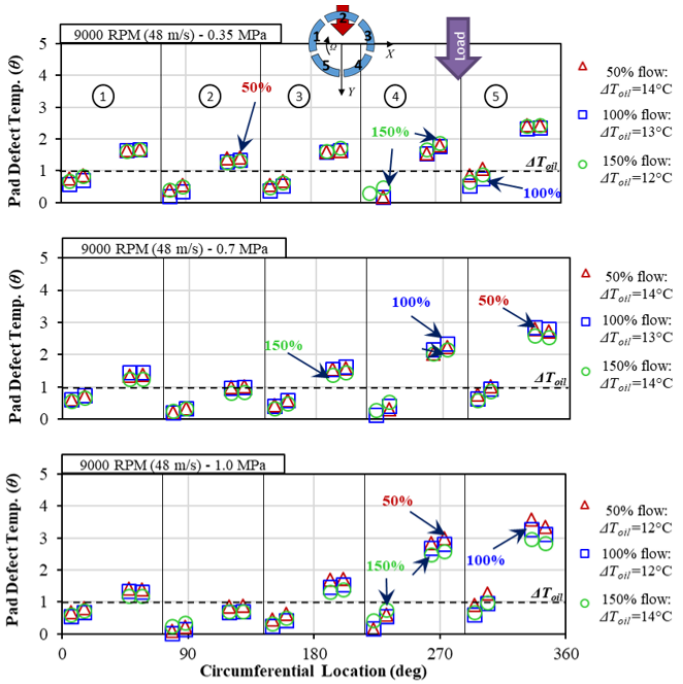

(a) 9 krpm (48 m/s)

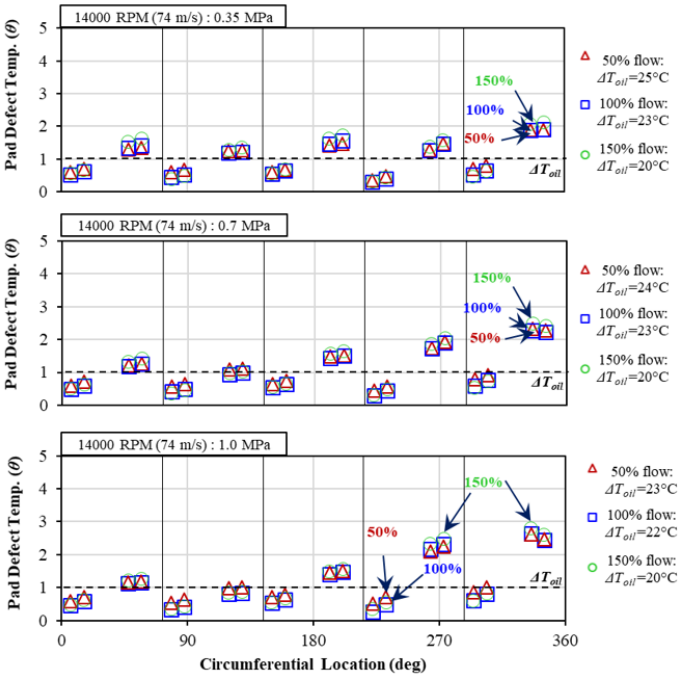

(b) 14 krpm (74 m/s)

Fig. 17. Measured pad defect temperature (*θ*) at 20 circumferential locations along mid-plane for operation at rotor speed (a) 9 krpm and (b) 14 krpm, under specific load (top) 0.35 MPa, (middle) 0.7 MPa and (bottom) 1.0 MPa, and three oil flow rates (50%, 100% and 150%).

Experimental Dynamic Force Coefficients for Test Bearing

After completing the bearing steady state performance measurements, an automated process performs a dynamic load excitation test by delivering multiple-frequency pseudo-random displacement signals to each shaker and measuring the dynamic response from the eddy-current sensors, force sensor and accelerometers [9].

The identification of bearing force coefficients requires first to find the bearing housing and support structure parameters in a dry (non-lubricated) condition and without shaft speed. The test bearing and its housing have an equivalent mass $M_S = 33 \pm 4$ kg, and the (rods) structure has stiffness $K_{Sx} = 1.2 \pm 1.2$ MN/m, $K_{Sy} = 3.5 \pm 1.3$ MN/m, with remnant damping coefficients $C_{Sx} = C_{Sy} = 15 \pm 4$ kNs/m. The flexibly suspended floating bearing system has a natural frequency $f_n = 220$ Hz and its damping ratio $\zeta = 0.02$ [8].

Next, oil lubricates the bearing and the procedure waits for thermal equilibrium; see Fig. 6 and discussionDuring the dynamic load tests, one shaker head (x direction) excites the seal housing with unidirectional multiple frequency pseudo-random forces $\mathbf{F_x} = [f_x = \Sigma\, f_o\, e^{i\omega t}, f_y = 0]^T$ to produce dynamic shaft motions $\mathbf{z_x} = [X_x, Y_x]^T$ and bearing accelerations $\mathbf{a_x} = [a_{xx}, a_{yx}]^T$. See Fig. 1 for the coordinate system and note i is the imaginary unit. After the x-shaker stops, the y-shaker repeats the excitation $\mathbf{F_y} = [f_x = 0, f_y = \Sigma\, f_o\, e^{i\omega t}]^T$ to produce the bearing displacements $\mathbf{z_y} = [X_y, Y_y]^T$ and acceleration $\mathbf{a_y} = [a_{XY}, a_{YY}]^T$.

Rouvas and Childs [16] detail the parameter identification procedure in the frequency domain. First, a Discrete Fourier Transformation method transfers the recorded time domain data into the frequency domain, say $\mathbf{F_{x(\omega)}} = \text{DFT}(\mathbf{F_{x(t)}})$. Next, define (2x2) matrices in the frequency domain as: force $\mathbf{F}_{(\omega)} = [\mathbf{F_{x(\omega)}} \mid \mathbf{F_{y(\omega)}}]$, housing acceleration $\mathbf{A}_{(\omega)} = [\mathbf{A_{x(\omega)}} \mid \mathbf{A_{Y(\omega)}}]$, and rotor relative displacements $\mathbf{Z}_{(\omega)} = [\mathbf{Z_{x(\omega)}} \mid \mathbf{Z_{y(\omega)}}]$. The test system has a complex stiffness matrix ($\mathbf{H}$) determined from

$$\mathbf{H}_{(\omega)} = [\mathbf{F}_{(\omega)} - M_S\, \mathbf{A}_{(\omega)}]\, \mathbf{Z}_{(\omega)}^{-1} \tag{6}$$

Subtracting the structure force coefficients from the system $\mathbf{H}$ yields the test bearing dynamic complex stiffness

$$\mathbf{H}_B = \mathbf{H} - [\mathbf{K}_S + i\, \omega\, \mathbf{C}_S] \tag{7}$$

Next, the complex stiffness is reconstructed in terms of constant parameters; namely stiffness K, viscous damping C, and virtual mass M coefficients:

$$\mathbf{H}_{B(\omega)} \leftarrow [\mathbf{K} - \omega^2 \mathbf{M} + i\, \omega\, \mathbf{C}]_B \tag{8}$$

Note the (K,C,M) parameters are best fits representing the complex dynamic stiffness over a certain frequency range.

The data acquisition system (DAQ) samples at 10,000 Hz and a dynamic load shake of the bearing repeats 10 times, each time delivering 32 constructed (pseudo-random) waveforms with excitation frequencies ranging from 10 Hz to 300 Hz, in steps of 10 Hz [8]. A typical dynamic load test lasts about 75 s.

Refer to Jani [8] for details on evaluation of the uncertainty for each force coefficient, and the correlation factors for each curve fit as determined from Eq. (8), i.e.,

$$\text{Real}(H_{B\alpha\beta}) \rightarrow (K_{\alpha\beta} - \omega^2 M_{\alpha\beta}),\ \ \text{Ima}(H_{B\alpha\beta}) \rightarrow \omega\, C_{\alpha\beta,\ \alpha\beta=x,y} \tag{9}$$

Figure 18 presents the real and imaginary parts of the bearing complex dynamic stiffnesses, $(H_{ij})_{i,j=x,y}$, versus excitation frequency (ω) for operation at 12 krpm (64 m/s), specific load = 1.4 MPa, and with the bearing supplied with 100% nominal flow. The real parts of (H_{xx}, H_{yy}) decrease with frequency (ω), which indicates a mild softening effect of the bearing (positive virtual mass, M>0). The imaginary parts of (H_{xx}, H_{yy}) increase linearly with frequency (ω) up to 290 Hz. The slope of Ima(H_{xx}) and Ima(H_{yy}) indicates constant damping coefficients (C_{xx}, C_{yy}). In general, predictions based on Ref. [15] show lower dynamic stiffnesses, real and imaginary parts, compared to the experimental results.

From Ref. [8]; for operation at most shaft speeds (6 krpm - 16 krpm) and under light loads (< 1.0 MPa), Real(H_{xx}) ≈ Real(H_{yy}); whereas at high loads, Real(H_{yy}) > Real(H_{xx}). The real part of the bearing cross-coupled complex stiffnesses, Real(H_{xy}) ≈ Real(H_{yx}), remains fairly constant, low in magnitude, both having negative signs for operation at rotor speeds from 6 krpm to 16 krpm, and under specific loads from 0.35 MPa to 2.1 MPa. For operation at rotor speeds from 3 krpm to 6 krpm, Im(H_{yy}) is slightly higher than Im(H_{xx}), whereas at rotor speeds > 9 krpm, Ima(H_{xx}) ≈ Ima(H_{yy}). The cross-coupled Ima(H_{xy}) and Ima(H_{yx}) have a low magnitude (near zero), both having negative signs.

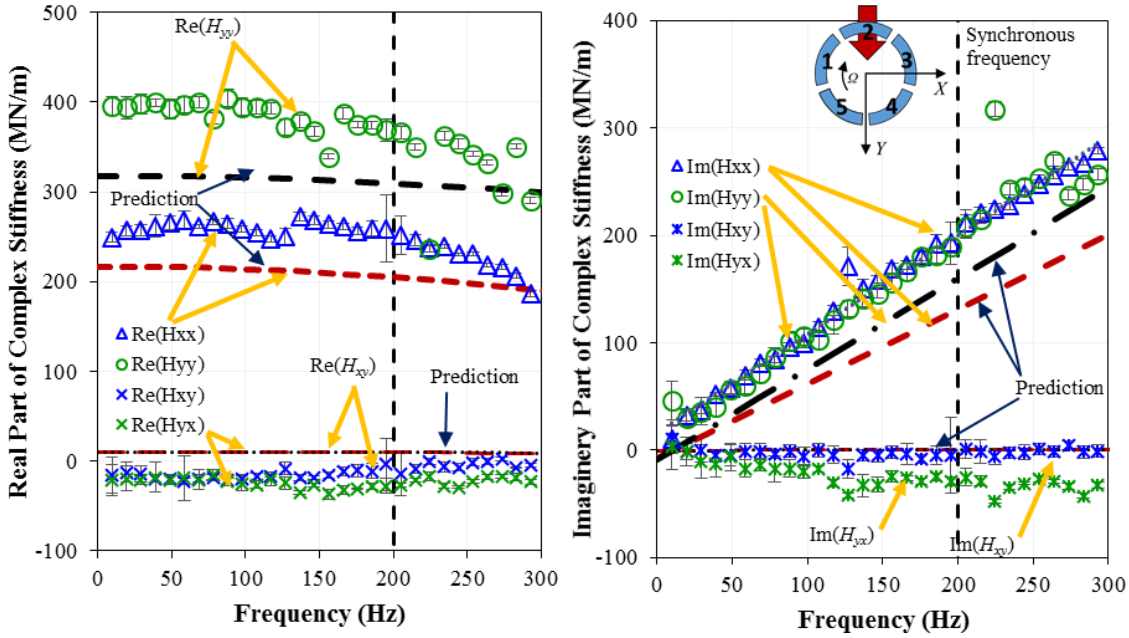

(a) Re(*H*) (b) Ima*(H)*

Fig. 18. Real and imaginary parts of test bearing complex dynamic stiffnesses $(H_{ij})_{i,j=x,y}$. Symbols: experiments, lines: predictions [15]. Operation at 12 krpm (64 m/s), 1.4 MPa specific load, and 100% nominal flow.

The identification process delivers the complex dynamic stiffness coefficients (H) and a curve fitting produces twelve force coefficients; four stiffnesses K and four virtual-masses M, and four damping coefficients C. In dimensionless or normalized form, define

$$k_{\alpha\beta} = K_{\alpha\beta}\frac{C_r}{W},\ c_{\alpha\beta} = C_{\alpha\beta}\frac{C_r\,\Omega}{W},\ m_{\alpha\beta} = m_{\alpha\beta}\frac{C_r\,\Omega^2}{W},\quad \alpha,\beta=x,y \tag{10}$$

where W is the applied static load and Ω is the shaft speed (rad/s).

Test Bearing Stiffness Coefficients. Figure 19 depicts the experimental direct stiffnesses k_{xx} and k_{yy} vs. shaft speed for increasing specific loads. The test bearing is supplied with the 100% nominal flow rate. Recall the y-axis denotes the direction of the applied load. Notably, $k_{yy} > k_{xx}$ for large specific loads ≥ 0.7 MPa. Both k_{xx} and k_{yy} are sensitive to an increase in rotor speed; however, k_{xx} varies more than k_{yy} under a light specific load.

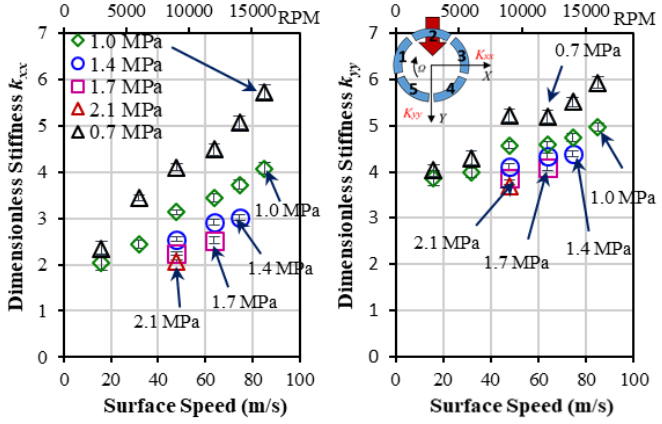

(a) k_{xx} (b) k_{yy}

Fig. 19. Test bearing dimensionless direct stiffnesses k_{xx} and k_{yy} vs. surface speed (16 m/s to 85 m/s) for operation at five specific loads (0.7 MPa to 2.1 MPa) and 100% nominal flow rate.

For instance, at a specific load of 1.0 MPa, k_{xx} increases by 95% with an increase in surface speed from 16 to 85 m/s, whereas k_{yy} increases by 30%. Do note the physical magnitude of the bearing stiffnesses increases with applied load, see Eq. (10). Jani (8) states the uncertainty for the bearing stiffnesses ranges from 1% to 5% of their magnitude thus showing a good precision of the measurements.

Figure 20 presents the experimental and predicted stiffnesses (k) vs. Sommerfeld number (S) for the same conditions detailed in Fig. 19. Labels on the figure borders denote the physical conditions; for example, a high load or a low speed determine a small S. Both k_{xx} and k_{yy} increase with S; whereas the cross-coupled stiffnesses k_{xy} and k_{yx} are quite small in magnitude. For $S < 2$, $k_{yy} < k_{xx}$; whereas for $S > 2$, $k_{xx} \approx k_{yy}$. The TEHD model predictions correlate well with k_{xx} and k_{yy} for $S < 4$, and under predict by up to 27% at $S = 4.6$, the condition with a small applied load of 0.35 MPa as circled in the graphs. Do note this operating condition delivers the smallest physical stiffnesses K_{xx} and K_{yy}.

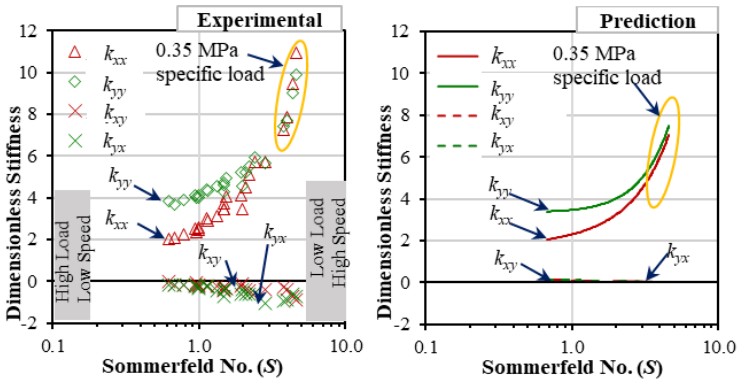

Fig. 20. Bearing experimental and predicted dimensionless stiffnesses (k_{xx}, k_{yy}) vs. Sommerfeld number (S) for operation at various shaft surface speeds (16 m/s-85 m/s) and specific loads (0.35 MPa-2.1 MPa).

For operation with the test bearing supplied with oil flow rate at 50%, 100% and 150% of nominal flow, Figure 21 depicts the stiffnesses k_{xx} and k_{yy} vs. surface speed and increasing applied loads (left to right graphs). In general, the bearing stiffnesses k_{xx} and k_{yy} slightly increase (or remain invariant) as the flow rate changes over a wide range. For operation at 9 krpm (48 m/s) and under a 1.0 MPa specific load, k_{xx} and k_{yy} are larger by ~5% and ~10%, respectively, for a 50% of nominal flow as compared to the coefficients for 100% nominal flow. Moreover, with an increase in oil flow (150% of nominal flow), the k's reduce by 1% to 5% or change insignificantly. The direct stiffnesses have a greater dependency on oil flow changes under at light specific load (<0.35 MPa) rather than at higher specific loads >0.7 MPa.

Test Bearing Damping Coefficients. Figure 22 presents the experimental direct damping coefficients c_{xx} and c_{yy} vs. shaft surface speed and specific load with the bearing supplied at the 100% nominal flow rate. For most operating cases, $c_{xx} \approx c_{yy}$. Note both coefficients c_{xx} and c_{yy} increase with shaft surface speed and decrease with an increase in specific load due to their normalization, Eq. (10). In physical magnitude, the damping coefficients are rather constant with applied load and slightly decrease as shaft speed increases. Overall, the experimental uncertainty for the direct damping coefficients ranges from 3% to 18% of their actual magnitude.

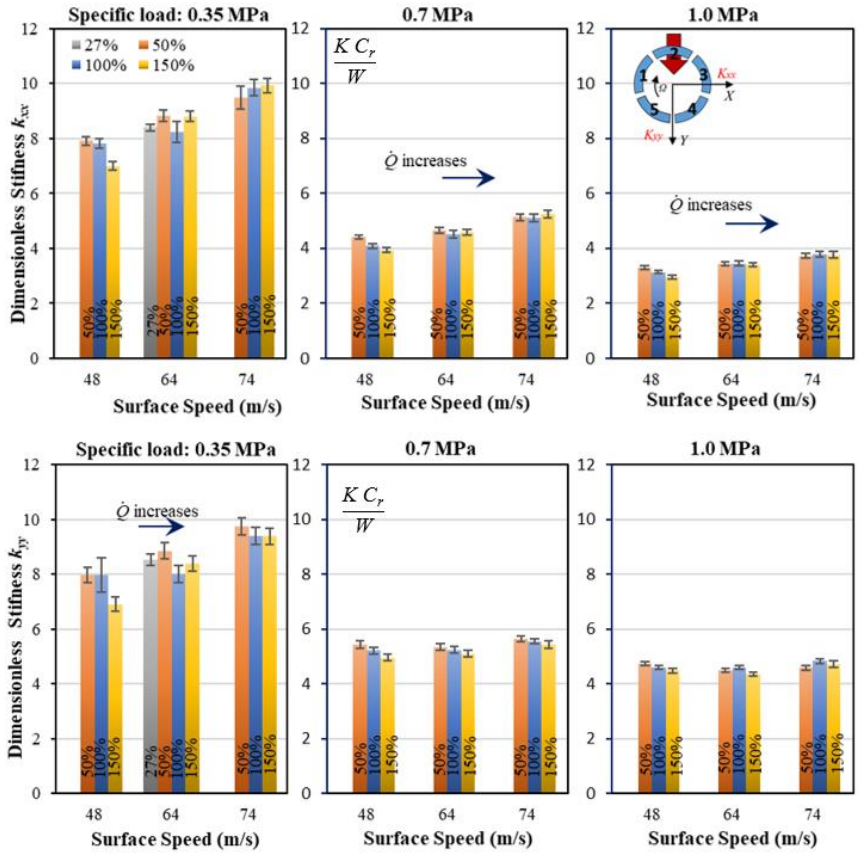

Fig. 21. Test bearing dimensionless stiffnesses (top) k_{xx} and (bottom) k_{yy} vs. shaft surface speed (m/s) for operation under specific loads 0.35 MPa, 0.7 MPa and 1.0 MPa (left to right), and bearing supplied with 50%, 100%, and 150% flow rates.

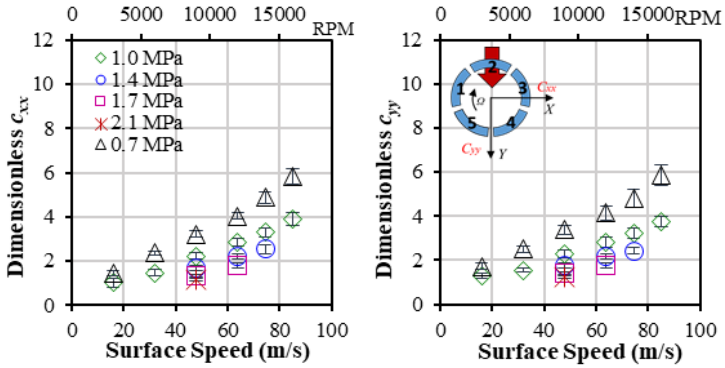

(a) c_{xx} **(b) c_{yy}**

Fig. 22. Test bearing dimensionless damping coefficients $_{xx}$ and c_{yy} vs. shaft surface speed (m/s) for operation at five specific loads (0.7 MPa to 2.1 MPa) and 100% nominal flow.

Figure 23 presents the experimental and predicted damping coefficients c_{xx} and c_{yy} vs. Sommerfeld number (S) for various test conditions in shaft surface speed and applied load. The bearing is lubricated with the nominal flow rates. Note $c_{xx} \approx c_{yy}$ over the entire S range. The predictive model produces damping coefficients agreeing well with the test data for $S < 3$. On the other hand, the model under predicts damping for $S > 3$, in particular for the condition with the lightest load W=0.35 MPa as circled in both graphs.

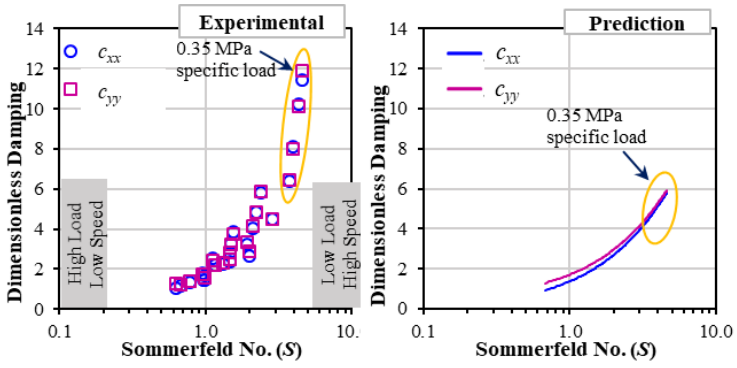

(a) Experimental (b) Predicted

Fig. 23. Bearing experimental and predicted dimensionless damping coefficients (c_{xx}, c_{yy}) vs. Sommerfeld number (S) for operation at various shaft speeds (16 m/s-85 m/s) and specific loads (0.35 MPa-2.1 MPa).

For operation with the test bearing supplied with oil flow rate at 50%, 100% and 150% of nominal flow, Figure 24 depicts the damping coefficients c_{xx} and c_{yy} vs. surface speed and increasing applied loads (left to right graphs). For a 50% nominal flow, c_{xx} and c_{yy} reduce by at most 7% compared to the coefficients obtained with a 100% nominal flow. In a worst case, c_{xx} and c_{yy} reduce by 16% for operation with a 27% nominal flow. Moreover, when over flooded (150% flow), c_{xx} and c_{yy} increase between 5% -10% max. at a shaft surface speed of 64 m/s and remain fairly constant or change randomly at other shaft surface speeds (48 and 74 m/s). The moderate changes in the damping coefficients as the flow varies are a result of the bearing flooded configuration that does prevent the bearing film lands to starve.

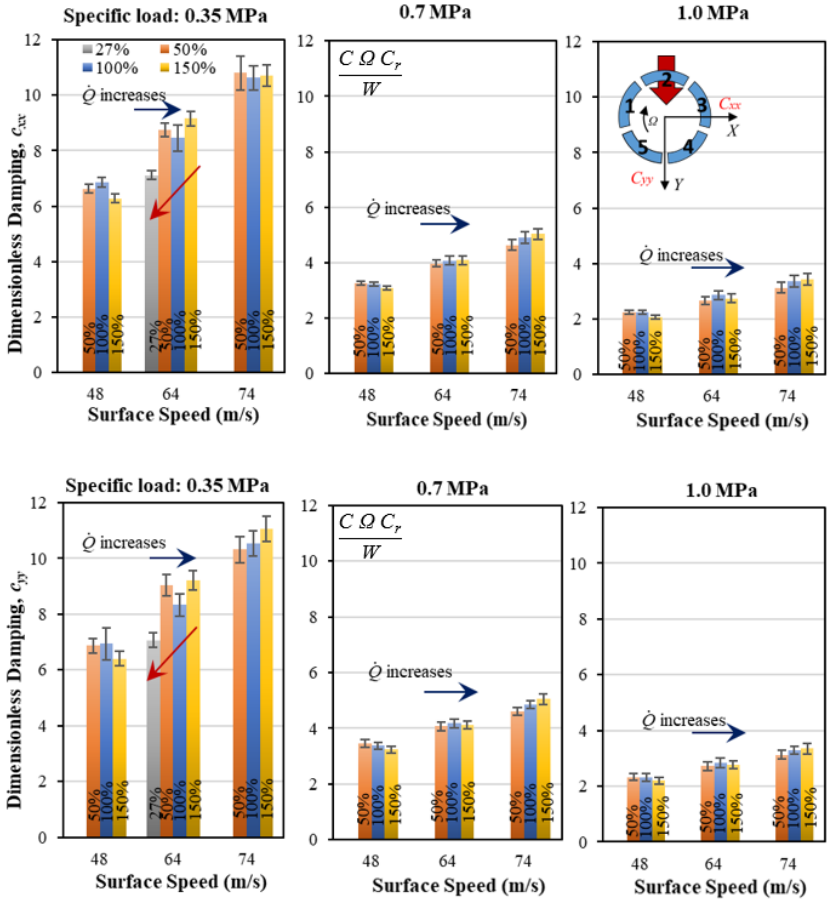

Fig. 23. Test bearing dimensionless damping coefficients (top) c_{xx} and (bottom) c_{yy} vs. shaft surface speed (m/s) for operation under specific loads 0.35 MPa, 0.7 MPa and 1.0 MPa (left to right), and bearing supplied with 50%, 100%, and 150% flow rates.

The mass coefficients m_{xx} and m_{yy} are not presented here as they produce a modest reduction (small %) of the dynamic stiffness at a frequency synchronous with shaft speed (ω=Ω) . Refer to Jani [8] for a complete description of the results found.

Do realize, from Figs. 20 and 23 that the normalized force coefficients (k, c), experimental and predicted, collapse into well-defined regions that fully correlate with the Sommerfeld number (S). This observation indicates that the performance of a TPJB can be normalized (as it was done until the recent past, the 20th century), in spite of changes in shaft surface speed or applied load. The experimental results thus give credence to well established principles in lubrication theory.

CONCLUSION

This lecture presents the measurement of the static and dynamic forced characteristics of a five-pad spherical pivot tilting-pad journal bearing (TPJB), flooded construction with end seals, under a load between pads (LBP) orientation. The work quantifies the influence of sizable variations in the oil supply flow rate into the performance of the test bearing measured for shaft surface speeds from 32 m/s to 85 m/s and specific loads from 0.17 MPa to 2.1 MPa. The nominal oil flow rate supplied to the bearing is nearly proportional to the shaft speed, i.e., not a constant throughout the test campaign.

The paper presents the experimental results and predictions, steady-state load and dynamic force coefficients, in a non-dimensional or normalized form that clusters trends in performance, as a function of the Sommerfeld number (S), in spite of the wide range of parameters varied; namely shaft speed, applied load and supplied flow. The display of information intends to educate and generalize the experimental results.

For operation with shaft surface speed up to 74 m/s (14 krpm) and specific load of 1.0 MPa, a 50% reduction in the nominal supply oil flow rate to the flooded bearing causes a minor increase in the measured shaft eccentricity, a moderate raise in pads' sub-surface temperatures up to 6°C, a 15% decrease in drag power loss, a 6% increase in direct stiffness, and a 7% reduction in direct damping. The flooded test bearing supplied with just 50% of the nominal oil flow delivers significant energy savings without overly high pad temperatures that could risk Babbitt layer failure, for example. On the other hand, an increase in supply oil flow rate, 50% above nominal, produces a 9% increase in drag power losses, a moderate reduction in pad sub-surface temperatures of up to 3°C, a 5% decrease in direct stiffness, and a maximum 10% increase in direct damping coefficients.

The current experimental procedure directly measures the drag torque to produce the bearing drag power losses, and which are correlated to the power loss derived from a common method using the measured oil flow rate and the lubricant temperature rise across the bearing. The exhaustive correlations displayed demonstrate that the simple method over predicts the drag power for operation with the nominal oil supply flow, while producing an (artificial) too low drag power loss for the condition of a reduced flow rate, 50% of the nominal condition.

The in-house TEHD prediction model [14,15] predicts accurate maximum pad temperatures on the loaded pads for shaft surface speeds ≥ 64 m/s (12 krpm), and also the journal eccentricity for shaft surface speeds ≥ 48 m/s (9 krpm). Moreover, the model predicts accurate stiffness and damping coefficients for Sommerfeld # $S < 2$ and under predicts both, stiffness and damping, for $S > 2$.

ACKNOWLEDGEMENT

The authors are thankful to the Elliott Group for their financial support and allowing the publication of the test data in this paper.

NOMENCLATURE

a_x, a_y	Bearing stator accelerations along x and y axis [m/s^2]
C_r	Radial bearing clearance [m]
$C_{S\alpha}$	Damping of support structure [Ns/m]
$C_{\alpha\beta}$	Bearing damping coefficients, α,β=x,y [Ns/m] , $c_{\alpha\beta}$=$C_{\alpha\beta}$ (C_r Ω/W)
D	Shaft or journal diameter [m]
e	Journal eccentricity [m]
F_x, F_y	Dynamic excitation force [N]
$H_{B\alpha\beta}$	Complex dynamic stiffness of bearing, α,β=x,y [N/m]
i	Imaginary unit [=]
$K_{S\alpha}$	Stiffness of support structure [N/m]
$K_{\alpha\beta}$	Bearing stiffness coefficients, α,β=x,y [N/m], $k_{\alpha\beta}$=$K_{\alpha\beta}$ (C_r/W)
L	Bearing pad axial length [m]
$M_{S\alpha}$	Mass of bearing and its support carrier [kg]
$M_{\alpha\beta}$	Bearing virtual-mass coefficients, α,β=x,y [kg], $m_{\alpha\beta}$=$M_{\alpha\beta}$ (C_r Ω^2/W)

n_p Number of pads on bearing.
$P_{estimated}$ Estimate of drag power loss based on temperature rise, Eq. (1) [W]
P_{lub} Theoretical estimation of drag power loss, Eq. (3) [W]
$P_{measured}$ Bearing drag power loss derived from measured drag torque and shaft rotational speed [W]
$\bar{P}$ $P_{measured\ or\ estimated} / P_{lub}$. Normalized bearing power loss
$\dot{Q}$ Lubricant supplied flow rate to bearing [m^3/s]
R ½ D. Journal radius [m]
S Sommerfeld number, Eq. (4)
T, T_{pad} Lubricant temperature and pad temperature [ºC]
T_{eff} $[T_{in} + ¾ (T_{exit} - T_{in})]$. Oil effective temperature [ºC].
T_{in}, T_{exit} Oil inlet and exit temperatures [ºC]
W Applied static load along y direction [N]
x,y coordinate system for displacement of shaft center [m]
z_x, z_y Bearing displacement relative to rotor [m]
β_p Pad arc length = 1.09 rad (63º)
ΔT $(T-T_{in})$. Temperature rise relative to oil inlet temperature [ºC]
ε e/C_r Journal eccentricity ratio [-]
μ Fluid viscosity [Pa.s]
μ_{eff} Oil viscosity at an effective temperature [Pa.s]
κ Fraction of drag power advected by lubricant flow [-]
θ Pad sub-surface defect temperature, Eq. (6) [-]
Ω, ω Rotor angular speed [rad/s], whirl frequency [rad/s]

Abbreviations

DAQ Data Acquisition System
DFT Discrete Fourier Transform
HC *Hot* Clearance
SSV Subsynchronous shaft vibrations
TPJB Tilting pad journal bearing
DE, NDE Drive end, non-drive end of bearin
CC *Cold* Clearance
LBP Load between pad configuration
TEHD Thermo-elasto-hydrodynamic

REFERENCES

[1] Nicholas, J. C., 1994, "Tilting Pad Bearing Design - Tutorial," *Proc. 23rd Turbomachinery Symposium*, The Turbomachinery Laboratory, Texas A&M University, September 13-15, Dallas, TX, USA, pp. 179-194, https://doi.org/10.21423/R11H2H

[2] DeCamillo, S., He, M., Cloud, C. H., and Byrne, J. M., 2008, "Journal Bearing Vibration and SSV Hash," *Proc. 37th Turbomachinery Symposium*, The Turbomachinery Laboratory, Texas A&M University, September 7-11, Houston, TX, USA, pp. 179-194, https://doi.org/10.21423/R1DH1J

[3] Whalen, J. K., He, M., Cerny, V., and Polreich, V., 2015, "The Effects of Starvation on the Dynamic Properties of Tilting Pad Journal Bearings," *Proc. 44th Turbomachinery Symposium*, The Turbomachinery Laboratory, Texas A&M University, September 14-17, Houston, TX, USA, pp. 1-10, https://doi.org/10.21423/R13922

[4] Heshmat, H., and Pinkus, O., 1985, "Performance of Starved Journal Bearings With Oil Ring lubrication," ASME *J Tribol*, **107**, pp. 23-31, https://doi.org/10.1115/1.3260998

[5] DeCamillo, S., and Brockwell, K., 2001, "A Study of Parameters that affect Pivoted Shoe Journal Bearing Performance in High-Speed Turbomachinery," *Proc. 30th Turbomachinery Symposium*, The Turbomachinery Laboratory, Texas A&M University, September 17-20, Houston, TX, USA, pp. 9-22, https://doi.org/10.21423/R1PW8G

[6] Dmochowski, W., and Blair, B., 2006, "Effect of Oil Evacuation on the Static and Dynamic Properties of Tilting Pad Journal Bearings," STLE *Trib Trans*, **49**, pp. 536-544, https://doi.org/10.1080/10402000600885175

[7] Nichols, B. R., Fittro, R. L., and Goyne, C. P., 2018, "Subsynchronous Vibration Patterns Under Reduced Oil Supply Flow Rates," ASME *J Eng Gas Turbines Power*, **140**(10): 102503, https://doi.org/10.1115/1.4038363

[8] Jani, H., 2018, "Measurements of the Static and Dynamic Force Performance on a Five-Pad, Spherical-Pivot Tilting-Pad Journal

Bearing: Influence of Oil Flow Rate", M.S. Thesis, Mechanical Engineering, Texas A&M University, College Station, TX, USA

[9] Coghlan, D. M., and Childs, D. W., 2017, "Characteristics of a Spherical Seat TPJB With Four Methods of Directed Lubrication: Part 1-Thermal and Static Performance," ASME *J Eng Gas Turbines Power*, **139**(12)

[10] De Choudhury, P., and Barth, E. W., 1981, "A Comparison of Film Temperatures and Oil Discharge Temperature for a Tilting-Pad Journal Bearing," ASME *J Lub Tech*, **103**(1), pp. 115–119. https://doi.org/10.1115/1.3251598

[11] Mitsui, J., Hori, Y., and Tanaka, M., 1983, "Thermohydrodynamic Analysis of Cooling Effect of Supply Oil in Circular Journal Bearing," ASME *J Lub Tech*, **105**(3), pp. 414-20. https://doi.org/10.1115/1.3254629

[12] De Choudhury, P., and Masters, D.A., 1984," Performance Tests of a Five-Shoe Tilting-Pad Journal Bearing," ASLE *Trans*, **27**(1), pp. 61-66, DOI: 10.1080/05698198408981545

[13] Pettinato, B., and De Choudhury, P., 1999, "Test Results of Key and Spherical Pivot Five-Shoe Tilt Pad Journal Bearings—Part I: Performance Measurements," STLE *Trib Trans*, **42**(3), pp. 541-547, DOI: 10.1080/10402009908982253.

[14] San Andrés, L., and Li. Y., 2015, "Effect of Pad Flexibility on the Forced Performance of Tilting Pad Journal Bearings: A Guide to Benchmarking a Predictive Model," ASME *J. Eng Gas Turbines Power*, **137** (12), 122503, https://doi.org/10.1115/1.4031344

[15] Abdollahi, B., and San Andrés, L, 2019, "Improved Estimation of Bearing Pads' Inlet Temperature: A Model , Against Test Data," ASME *J. Trib*, **141**(3), 031703, https://doi.org/10.1115/1.4041720

[16] Rouvas, C., and Childs, D.W., 1993, "A Parameter Identification Method for the Rotordynamic Coefficients of a High Reynolds Number Hydrostatic Bearing," ASME *J Vib Acoust*, **115**(3), pp. 264-270, https://doi.org/10.1115/1.2930343

